

ON THE NATURE OF PROMPT EMISSION, X AND GAMMA RAY FLARES AND EXTENDED THERMAL
EMISSION IN GRB 151027A

R. RUFFINI,^{1,2,3,4} Y. AIMURATOV,^{1,2} L. BECERRA,^{1,2} C. L. BIANCO,^{1,2} Y. C. CHEN,^{1,2} M. KARLICA,^{1,2,3}
M. KOVAČEVIĆ,^{1,2,3} J. D. MELON FUKSMAN,^{1,2} R. MORADI,^{1,2} M. MUCCINO,^{1,2} G. B. PISANI,^{1,2} D. PRIMORAC,^{1,2}
J. A. RUEDA,^{1,2,4} AND Y. WANG^{1,2}

¹*ICRA and Dipartimento di Fisica, Sapienza Università di Roma, P.le Aldo Moro 5, 00185 Rome, Italy*

²*ICRANet, P.zza della Repubblica 10, 65122 Pescara, Italy.*

³*Université de Nice Sophia Antipolis, CEDEX 2, Grand Château Parc Valrose, Nice, France*

⁴*ICRANet-Rio, Centro Brasileiro de Pesquisas Físicas, Rua Dr. Xavier Sigaud 150, 22290-180 Rio de Janeiro, Brazil. ruffini@icra.it*

ABSTRACT

We here identify GRB 151027A as a binary-driven hypernova (BdHN): a long GRB with progenitor a carbon-oxygen core (CO_{core}), on the verge of supernova (SN) explosion, and a binary companion neutron star (NS). The hypercritical accretion of the SN ejecta on the companion NS leads to the gravitational collapse of the NS into a black hole and, in sequence, the emission of the GRB and a copious e^+e^- plasma. Here we follow the impact of the e^+e^- plasma on the SN ejecta with the consequent emission of the two peaks of the prompt radiation, the double emission composed by the Gamma-ray flare and the X-ray flare. We proceed first to the description of these two double component generalizing our recent works, performing the time integrated and time resolved analysis for the prompt emission phase, confirming its ultra relativistic nature and confirming as well the mildly relativistic nature of the Gamma-ray flares and X-ray flares. We also confirm the presence of announced X-ray thermal emission and confirm our recent proposal that this emission occurs in the transition from a SN to an HN: we here give the needed details. We then enter into the theoretical justification of these observations by integrating the hydrodynamical equations corresponding to the propagation e^+e^- into the SN ejecta simulated by 3D smoothed particle like hydrodynamics. We compare and contrast our results with analysis based on the collapsar-fireball-single jetted ultra-relativistic emission.

Keywords: gamma-ray burst: general — binaries: general — stars: neutron — supernovae: general
— black hole physics — hydrodynamics

1. INTRODUCTION

Gamma-ray bursts (GRBs) are traditionally classified in short GRBs, with a total duration $\lesssim 2$ s, and long GRBs, lasting $\gtrsim 2$ s (Mazets et al. 1981; Dezalay et al. 1992; Klebesadel 1992; Kouveliotou et al. 1993; Tavani 1998). The large majority of long bursts is spatially correlated with bright star-forming regions in their host galaxies (Fruchter et al. 2006; Svensson et al. 2010). For this reason the long GRBs have been traditionally associated to the death of a single massive star, i.e., the *collapsar* (see Woosley & Bloom 2006, and references therein). However, the collapsar model contrasts with some observational facts: 1) most massive stars are found in binary systems (Smith 2014), 2) most type Ib/c SNe occur in binary systems (Smith et al. 2011) and 3) the SNe associated to long GRBs are indeed of type Ib/c (Della Valle 2011). Indeed, recently we have found evidence for multiple components in long GRB emissions indicating the presence of a precise sequence of different astrophysical processes (Izzo et al. 2012; Penacchioni et al. 2012), which led to reconsider and formulate in precise terms the physics and astrophysics of the Induced Gravitational Collapse (IGC) paradigm (Ruffini et al. 2001a, 2007; Rueda & Ruffini 2012; Fryer et al. 2014) making explicit the role of binary systems as progenitors of the long GRBs. Within the IGC scenario long bursts originate in tight binary systems composed of a carbon-oxygen core (CO_{core}) undergoing a SN explosion and a companion neutron star (NS) (Rueda & Ruffini 2012; Fryer et al. 2014; Becerra et al. 2015). The SN explosion triggers hypercritical accretion onto the companion NS (Rueda & Ruffini 2012; Fryer et al. 2014; Ruffini et al. 2016). In this process photons are trapped in the infalling material and the gravitational energy gained by accretion is carried out through an efficient neutrino emission (Zel’dovich et al. 1972; Ruffini & Wilson 1973; Fryer et al. 2014). Depending on the CO_{core} -NS binary separation/period two outcomes may occur. For widely separated ($a \gtrsim 10^{11}$ cm) CO_{core} -NS binaries, the hypercritical accretion rate is $< 10^{-2} M_{\odot} \text{ s}^{-1}$ and it is insufficient to induce gravitational collapse to a BH of the binary companion NS. Instead, the NS just increases its mass becoming a massive NS (MNS). This process leads to the emission of the so-called X-ray flashes (XRFs) with a typical X-ray emission $\lesssim 10^{52}$ erg. For more tightly bound ($a \lesssim 10^{11}$ cm) CO_{core} -NS binaries the hypercritical accretion rate of the SN ejecta can be $\gtrsim 10^{-2}$ – $10^{-1} M_{\odot} \text{ s}^{-1}$, leading the companion NS to collapse to a BH. This process leads to the occurrence of a binary-driven hypernova (BdHN) which exhibits a more complex structure than XRFs and an emission $\gtrsim 10^{52}$ erg (Ruffini et al. 2016).

An extensive analysis of BdHNe, with special application to the X-ray flares, can be found in (Ruffini et al. 2017b). There we have shown how the systematic use of the four different time coordinates, already indicated in Ruffini et al. (2001a), is needed for a correct relativistic formulation of the GRB phenomenon and leads to uncover new relations between the rest-frame peak time t_p , peak luminosity L_p , rest-frame duration Δt , total energy E_X of the X-ray flare and the prompt emission isotropic energy E_{iso} (Ruffini et al. 2017b). In the same paper we have shown that the relativistic analysis of a thermal emission observed in some X-ray flares gives crucial informations on the expansion of the SN ejecta: a mildly relativistic velocity $\approx 0.8c$ and an initial radius of $\approx 10^{12}$ cm (Ruffini et al. 2017b).

These results have already significantly modified the understanding of GRBs and have led to the implementation of a new visualization of the GRB phenomenon (see Fig. 1). One of the key points has been the introduction of a new space-time diagram which clearly evidences the very large number of new episodes and new physical processes, each with explicitly computed time varying Lorentz Γ factors, occurring in a GRB. The space-time diagram, as such, especially illustrate the departure from the traditional collapsar-fireball description of a GRB in terms of a single causally-related relativistic jet there described uniquely in the arrival time of the observer frame. Three important differences are made manifest. The first is the visualization of the GRB process in the cosmological rest frame of the source (see details in Ruffini et al. 2017b). The second is the description of the GRB in the “laboratory frame”, which allow to formulate a physical description centered on the BH and properly evaluate the causal connection. The third is that the prompt emission phase, the gamma-ray flare and the X-ray flare occur in a sequence only when parametrized in the arrival time and in fact *they are not* causally related. Fig. 1 also emphasizes that in the BdHNe where both gamma- and X-ray flares are present there is no evidence for GeV emission: the occultation by the hypernova ejecta makes the GeV emission unobservable. Such a special class of BdHNe corresponds to systems with a viewing angle co-planar with the orbital plane of the binary progenitor (Aimuratov, Y. et al., in preparation).

We here focus on the particular example of GRB 151027A. In this paper we adopt a stepwise approach progressively implementing the new regimes and the new episodes of the GRB phenomenon. We start from the well established ones, successfully adopted. In section 2 we summarize the relevant observations of GRB 151027A and perform the time-integrated analy-

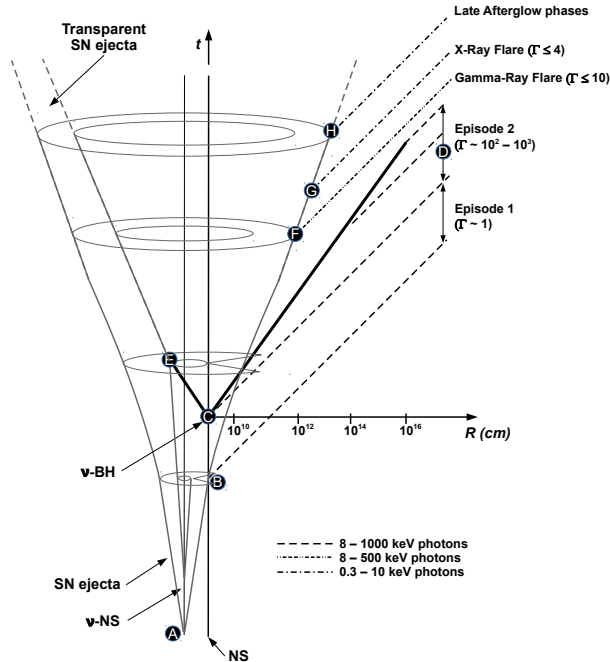


Figure 1. Space-time diagram (not in scale) of BdHNe. The CO_{core} explodes as a SN at point A and forms a new NS (ν NS). The companion NS (bottom right line) accretes the SN ejecta starting from point B, giving rise to the non-relativistic Episode 1 emission (with Lorentz factor $\Gamma \approx 1$). At the point C the NS companion collapses into a BH, and an e^+e^- plasma — the dyadosphere — is formed (Ruffini 1999). The following self-acceleration process occurs in a spherically symmetric manner (thick black lines). A large portion of plasma propagates in the direction of the line of sight, where the environment is cleared by the previous accretion into the NS companion, finding a baryon load $B \lesssim 10^{-2}$ and leading to the GRB prompt gamma-ray spikes (Episode 2, point D) with $\Gamma \sim 10^2-10^3$. The remaining part of the plasma impacts with the high density portion of the SN ejecta (point E), propagates inside the ejecta encountering a baryon load $B \sim 10^1 - 10^2$, and finally reaches transparency, leading to the Gamma-ray flare emission (point F) in gamma rays with an effective Lorentz factor $\Gamma \lesssim 10$ and to the X-Ray flare emission (point G) with an effective $\Gamma \lesssim 4$, which are then followed by the late afterglow phases (point H). For simplicity, this diagram is 2D and static and does not attempt to show the 3D rotation of the ejecta.

sis for the prompt emission, Gamma-ray flare and X-ray flare. In section 3 we perform the time-resolved analysis for the prompt emission, Gamma-ray flare and X-ray flare. In section 3.1 we analyze the two spikes in the prompt emission and apply to the first one the fireshell model we identify the P-GRB, the baryon load $B = (1.92 \pm 0.35) \times 10^{-3}$ and an average CBM density of $(15.9 \pm 3.2) \text{ cm}^{-3}$ which are consistent with our numerical simulation presented in Sec. 5, with the

Lorentz gamma factor $\Gamma_0 = 503 \pm 76$ confirming its ultra-relativistic nature. In section 3.2 The Gamma-ray flare is divided into 8 time intervals, we find an high significant thermal component existing in all time intervals (see Fig. 6), we report the results of our time-resolved spectral analysis in the first five column of Tab. 1. Using the best fit model for non-thermal component in the time interval 95-130 s we determine a Lorentz gamma factor of Gamma for the gamma ray flare duration. In section 3.3 The X-ray flare is analyzed in 4 time intervals, of which spectra are best fitted by a single power-law. In section 4 we turn to the thermal component evolving across the Gamma-ray flare by adopting the description in the GRB laboratory frame. Following our recent works (Ruffini et al. 2017b), we determine the expansion speed evidencing the transition from an initial velocity $\approx 0.38 c$ and increasing up to $0.98 c$ in the late part, see Tab. 1 column 6. This is the first relativistic treatment of the Gamma-ray flare and its associated thermal emission clearly evidencing the transition from a SN to an HN, identified in GRB 151027A. In section 5 we proceed to the Gamma-ray and X-ray flare theoretical explanation from the analysis of the e^+e^- plasma propagating within the SN ejecta. The simulated velocity and radius of the Gamma-ray and X-ray flare are consistent with the observation. In section 6, we proceed to visualize the conclusions by some simulated images recently jointly performed by our group in collaboration with the Los Alamos laboratory. This visualization is particularly helpful in order to appreciate the novel results made possible by the BdHN paradigm. The impact of the e^+e^- plasma on the entire SN ejecta gives origin to the thermal emission from the external surface of the SN ejecta. We finally compare and contrast our results with the alternative analysis by Nappo et al. (2017), based on the collapsar-fireball-single-jetted ultra-relativistic emission.

2. GENERAL PROPERTIES: TIME-INTEGRATED DATA ANALYSIS

GRB 151027A was detected and located by the *Swift* Burst Alert Telescope (BAT) (Maselli et al. 2015). It was also detected by the *Fermi* Gamma Burst Monitor (GBM) (Toelge et al. 2015), MAXI (Masumitsu et al. 2015) and by *KonusWind* (Golenetskii et al. 2015). The *Swift* X-Ray Telescope (XRT) started its observation 87 s after the burst trigger (Goad et al. 2015). The redshift of the source, measured through the MgII doublet in absorption from the Keck/HIRES spectrum, is $z = 0.81$ (Perley et al. 2015). The LAT boresight of the source was 10° at the time of the trigger, there are no associated high energy photons; an upper limit of

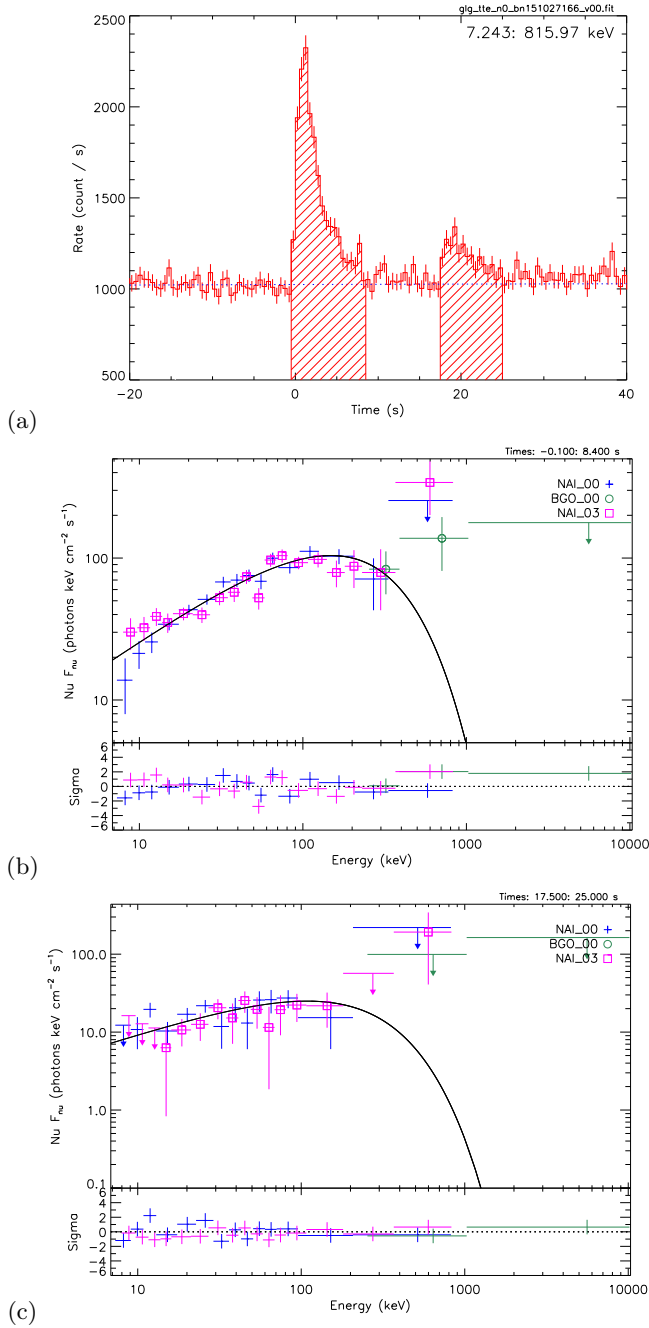


Figure 2. (a) The *Fermi*-GBM light curve from the Nal-n0 detector (≈ 8 –800 keV) of the prompt emission of GRB 151027A. The dotted horizontal line corresponds to the γ -ray background. (b) Time-integrated νF_ν spectrum of the first spike. (c) Time-integrated νF_ν spectrum of the second spike.

observed count flux is computed as 9.24×10^{-6} photons $\text{cm}^{-2} \text{s}^{-1}$ following the standard *Fermi*-LAT likelihood analysis. The BAT light curve showed a complex peaked structure lasting at least 83 seconds. XRT began observing the field 48 s after the BAT trigger. The GBM

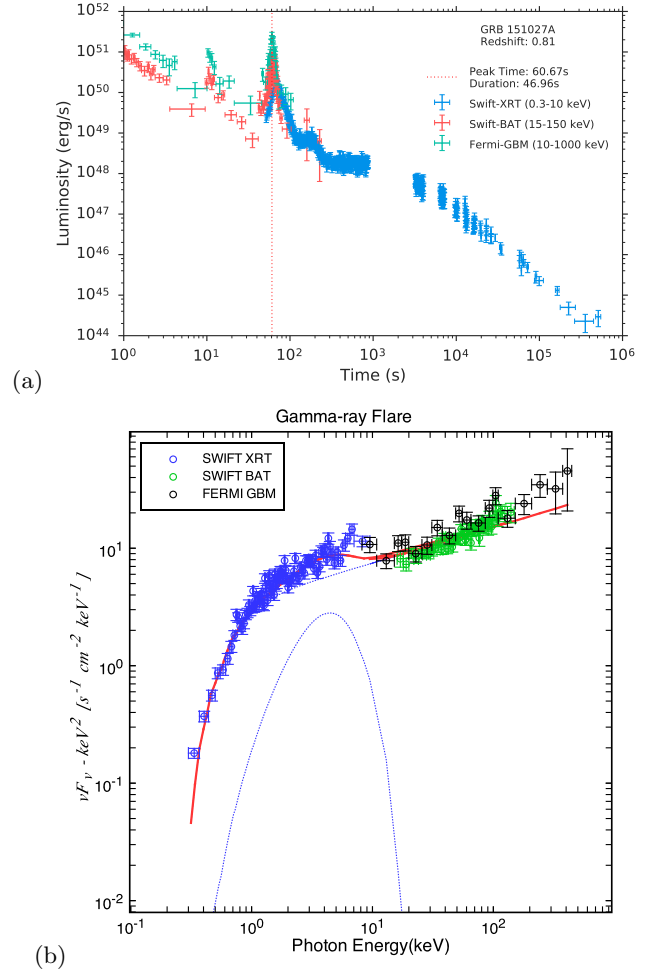


Figure 3. (a) Luminosity light curves in the rest-frame energy bands 10–1000 keV for *Fermi*-GBM (green), 15–150 keV for *Swift*-BAT (red), and 0.3–10 keV for *Swift*-XRT (blue). The red dotted line marks the position of the Gamma-ray flare. (b) Time-integrated νF_ν spectrum of the Gamma-ray flare and the PL+BB model (solid red curve) best-fitting the data.

light curve consists of various pulses with a duration of about 68 s in the 50–300 keV band. The *Konus-Wind* light curve consists of various pulses with a total duration of ~ 66 s. The *MAXI* detection is not significant, but the flux is consistent with the interpolation from the *Swift*/XRT light curve. This GRB composes:

- 1) The first 25 s (rest-frame 14 s) of emission corresponding to its prompt emission and encompassing two spikes of duration ≈ 8.5 s and ≈ 7.5 s, respectively (see Fig. 2 (a)). The rest-frame 1– 10^4 keV isotropic equivalent energies computed from the spectra of these two spikes (see Figs. 2 (b) and (c)) are $E_{\text{iso},1} = (7.26 \pm 0.36) \times 10^{51}$ erg and $E_{\text{iso},2} = (4.99 \pm 0.60) \times 10^{51}$ erg, respectively.

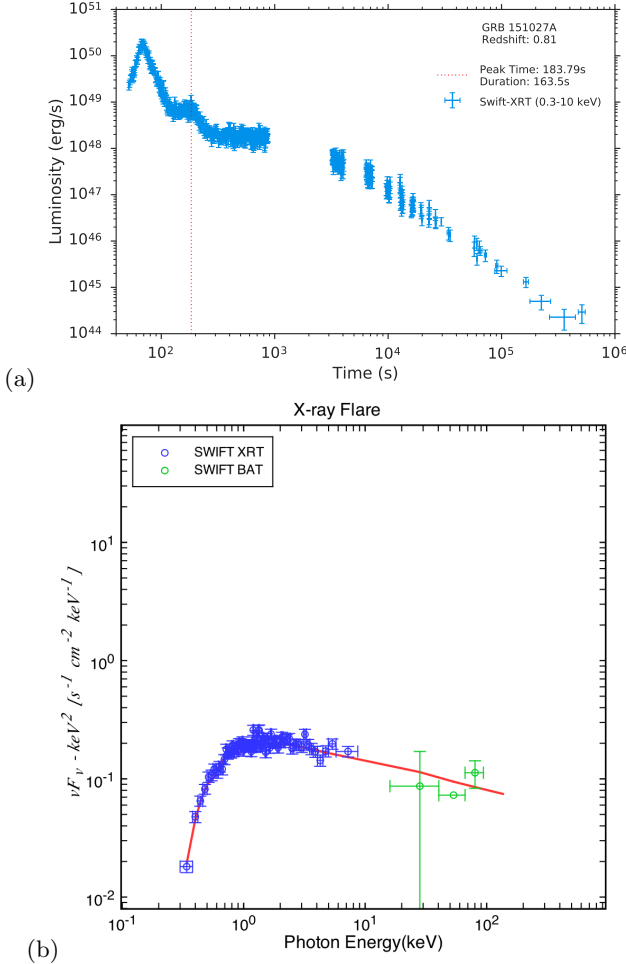


Figure 4. (a) Rest-frame 0.3–10 keV luminosity light curve of GRB 151027A. The red dotted line marks the position of the X-ray flare. (b) Time-integrated νF_ν spectrum of the X-ray flare and the PL model (solid red curve) best-fitting the data.

- 2) The Gamma-ray flare is observed in the time interval 94–180 s (corresponding to the rest-frame time interval 52–99 s, see Fig. 3 (a)). The luminosity light curves in the rest-frame energy bands 10–1000 keV for *Fermi*-GBM (green), 15–150 keV for *Swift*-BAT (red), and 0.3–10 keV for *Swift*-XRT (blue) are displayed. The total isotropic energy of the Gamma-ray flare is $E_\gamma = (3.28 \pm 0.13) \times 10^{52}$ erg. The overall spectrum is best-fit by a superposition of a power-law (PL) function with an index -1.69 ± 0.01 and a BB model with a temperature $kT = 1.13 \pm 0.08$ keV (see Fig. 3 (b)).
- 3) The X-ray flare, which has been discussed in Ruffini et al. (2017b), peaks at a rest-frame time $t_p = (184 \pm 16)$ s, has a duration $\Delta t = (164 \pm 30)$ s, a peak luminosity $L_p = (7.1 \pm 1.8) \times 10^{48}$ erg/s,

and a total energy in the rest-frame 0.3–10 keV energy range $E_X = (4.4 \pm 2.9) \times 10^{51}$ erg. The overall spectrum within its duration Δt is best-fit by a PL model with a power-law index of -2.24 ± 0.03 (see Fig. 4).

3. EVOLUTIONARY PROPERTIES: TIME-RESOLVED DATA ANALYSIS

We proceed to the time-resolved analysis of the prompt emission, the Gamma-ray flare, and the X-ray flare.

3.1. Prompt emission time-resolved analysis

We start the analysis of the first spike of GRB 151027A (see Fig. 2) as the traditional prompt emission of a long GRB within the fireshell model (see, e.g., Ruffini et al. 2003, for a review).

Thanks to the wide energy range of the *Fermi*-GBM instrument (8–1000 keV) it has been possible to perform a time-resolved analysis within the prompt emission phase to search for the typical GRB emission at the transparency of the e^+e^- -baryon plasma: the P-GRB characterized by a black body (BB) spectrum (Ruffini 1999; Ruffini et al. 2000, 2001b). Indeed, we find this thermal spectral feature in the time interval $T_0 - 0.1 - T_0 + 0.9$ s (with respect to the *Fermi*-GBM trigger time T_0). The best-fit model of this emission is a composition of a BB spectrum and a cut-off power-law model (CPL, see Fig. 5(a)). The BB component has an observed temperature $kT = (36.6 \pm 5.2)$ keV and an energy $E_{\text{BB}} = (0.074 \pm 0.038)E_{\text{iso},1} = (5.3 \pm 2.7) \times 10^{50}$ erg. These values are in agreement with the theoretical ones inferred from the fireshell model (Ruffini et al. 2010) for an initial e^+e^- plasma of energy $E_{e^+e^-}^{\text{tot}} \equiv E_{\text{iso},1}$, with a baryon load $B = (1.92 \pm 0.35) \times 10^{-3}$, and a Lorentz factor and a radius at the transparency condition of $\Gamma_0 = 503 \pm 76$ and $r_{\text{tr}} = (1.92 \pm 0.17) \times 10^{13}$ cm, respectively.

After the determination of the initial conditions for the fireshell, i.e., $E_{e^+e^-}^{\text{tot}}$ and B , we start the simulation of the first spike of the prompt emission (from $T_0 + 0.9$ s to $T_0 + 9.6$ s). In the fireshell model, this emission occurs after the P-GRB and results from the interaction of the accelerated baryons of the baryon load with the circumburst medium (CBM, Ruffini et al. 2002, 2006; Patricelli et al. 2012). To simulate the prompt emission light curve and its corresponding spectrum, we need to derive the number density of the CBM clouds surrounding the burst site. The agreement between the observations and the simulated light curve (see Fig. 5(b)) and the corresponding spectrum (see Fig. 5(c)) is obtained for an average CBM density of (15.9 ± 3.2) cm^{-3} (see

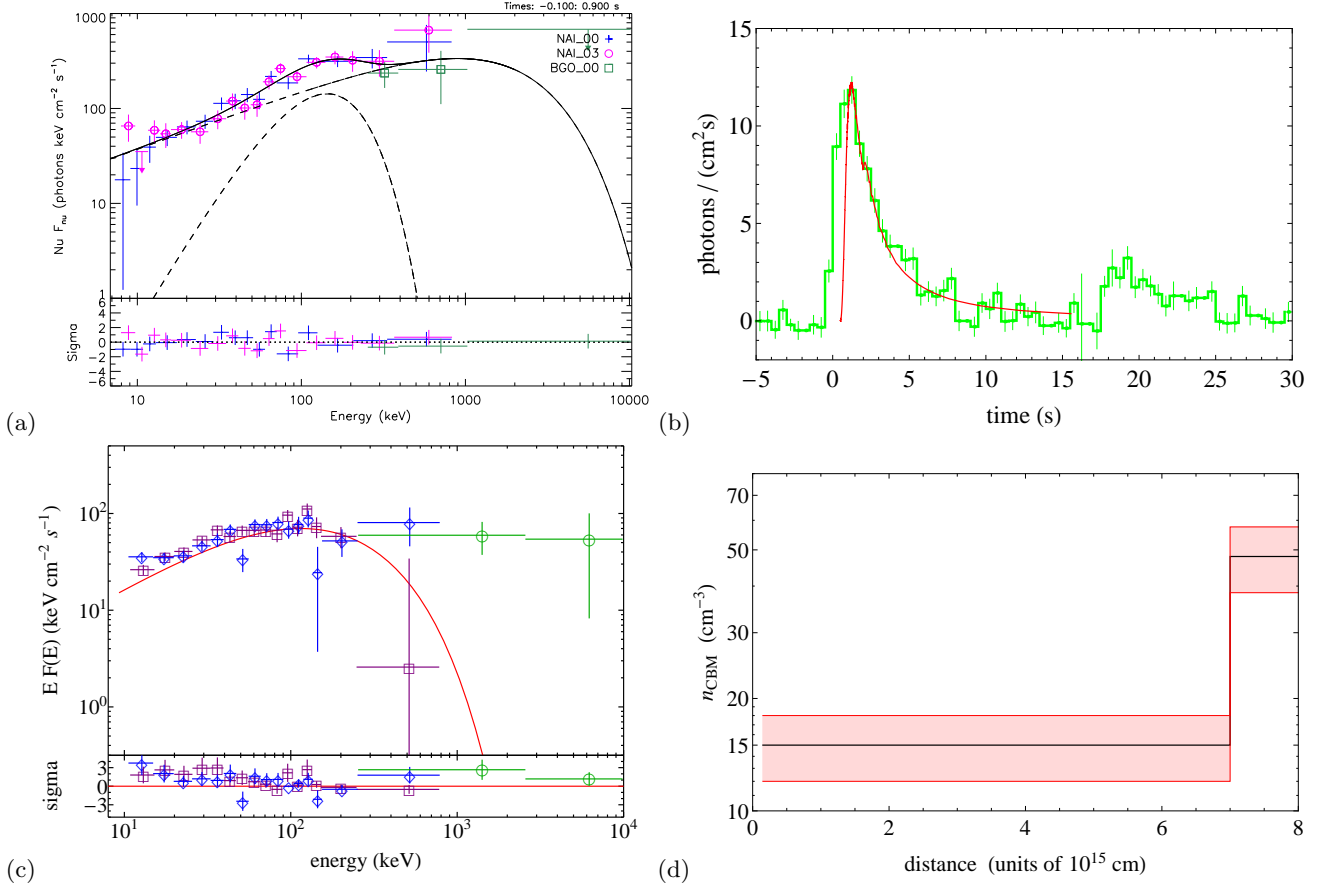


Figure 5. Prompt emission: (a) The combined NaI–n0, n3+BGO–b0 νF_ν spectrum of the P-GRB in the time interval $T_0 - 0.1 - T_0 + 0.9$ s. The best-fit model is CPL+BB. (b) The comparison between the background subtracted 10–1000 keV *Fermi*-GBM light curve (green) and the simulation with the fireshell model (red curve). (c) The comparison between the NaI–n0 (purple squares), n3 (blue diamonds) and the BGO–b0 (green circles) νF_ν data in the time interval $T_0 + 0 - 9 - T_0 + 9.6$ s and the simulated fireshell spectrum (red curve). (d) The radial density of the CBM clouds used for the above prompt emission light curve and spectrum simulations.

Fig. 5(d)) consistent with the simulation presented in Sec. 5, typical of the long burst host galaxies and the radius $\simeq 10^{16}$ cm. The second spike of the prompt emission appears to be featureless.

3.2. Gamma-ray flare time-resolved analysis

We perform a more detailed analysis by dividing the whole Gamma-ray flare duration (94–180 s) into 8 intervals (indicated with Δt_a^d in Tab. 1). Among these time intervals, the first 6 have both BAT and XRT data (total energy range 0.3–150 keV), while the last 2 fits involve XRT data only (energy range 0.3–10 keV). The XRT data were extremely piled-up and corrections have been performed in a conservative way to ascertain that the BB is not due to pile-up effects (Romano et al. 2006). The absorption of the spectrum below 2 keV has been also taken into due account. We use here the following spectral energy distributions to fit the data: power-law (PL), CPL, PL+BB and CPL+BB. An extra BB component is always preferred to the simple PL models and,

only in the sixth interval, to the CPL model whose cutoff energy may be constrained within 90% significance. The results of the time-resolved analysis are shown in Fig. 6 and summarized in Tab. 1. The BB parameters and errors in Tab. 1 correspond, respectively, to the main values and the 90% probability interval errors with respect to the central values, both obtained from Markov Chain–Monte Carlo method applied in XSpec with 10^5 steps (excluding first 10^4). The values are in line with the ones corresponding to minimum χ^2 and errors to the ones corresponding to intervals obtained from the difference $\Delta\chi^2 = 2.706$ from the minimum χ^2 value. The only exception is the first time bin where χ_{min}^2 value is almost two times lower than the main value. It is useful to infer the bulk Lorentz gamma factor of the Gamma-ray flare emission from the non-thermal component of the spectrum. Using the *Fermi* data, the best fit model for this non-thermal component in the time interval 95–130 s is a CPL with a spectral cutoff energy

Table 1. Gamma-ray flare: parameters of the time-resolved spectral analysis. Columns list respectively, the time interval of the spectral analysis, the PL or CPL index α , the CPL peak energy E_p when present, the BB observed temperature kT_{obs} and normalization A_{BB} , fitted from Sec. 3. The quantity ϕ_0 , the expansion speed β and the Lorentz factor Γ , and the effective thermal emitter radius in the laboratory frame R inferred from Sec. 4.

Δt_a^d (s)	Model	α	E_p (keV)	kT_{obs} (keV)	A_{BB} ($\text{ph cm}^{-2}\text{s}^{-1}$)	ϕ_0 (10^{12} cm)	β	Γ	R (10^{12} cm)
94–100	BB+PL	$1.349^{+0.024}_{-0.036}$		$2.2^{+1.1}_{-1.1}$	$0.052^{+0.043}_{-0.034}$	$0.065^{+0.070}_{-0.064}$	$0.38^{+0.19}_{-0.31}$	$1.079^{+0.138}_{-0.077}$	$0.10^{+0.11}_{-0.10}$
100–110	BB+PL	$1.293^{+0.029}_{-0.031}$		$2.57^{+0.43}_{-0.50}$	$0.206^{+0.083}_{-0.084}$	$0.094^{+0.037}_{-0.041}$	$0.606^{+0.042}_{-0.049}$	$1.257^{+0.057}_{-0.053}$	$0.194^{+0.077}_{-0.086}$
110–120	BB+PL	$1.392^{+0.028}_{-0.033}$		$2.17^{+0.22}_{-0.26}$	$0.62^{+0.14}_{-0.15}$	$0.229^{+0.053}_{-0.062}$	$0.852^{+0.035}_{-0.052}$	$1.91^{+0.26}_{-0.24}$	$0.80^{+0.21}_{-0.25}$
120–130	BB+PL	$1.732^{+0.049}_{-0.057}$		$1.10^{+0.14}_{-0.12}$	$0.592^{+0.077}_{-0.073}$	$0.87^{+0.23}_{-0.20}$	$0.957^{+0.014}_{-0.028}$	$3.46^{+0.78}_{-0.76}$	$5.7^{+1.8}_{-2.3}$
130–140	BB+PL	$1.82^{+0.11}_{-0.14}$		$0.617^{+0.046}_{-0.043}$	$0.247^{+0.037}_{-0.038}$	$1.79^{+0.30}_{-0.28}$	$0.983^{+0.0046}_{-0.0079}$	$5.6^{+1.0}_{-1.0}$	$19.1^{+4.2}_{-5.6}$
140–150	CPL+PL	$1.65^{+0.15}_{-0.16}$	$7.3^{+66.3}_{-4.6}$	$0.469^{+0.065}_{-0.064}$	$0.102^{+0.028}_{-0.027}$	$1.99^{+0.61}_{-0.61}$	$0.919^{+0.054}_{-0.560}$	$2.5^{+1.8}_{-1.5}$	$9.5^{+4.4}_{-9.5}$
150–160	BB+PL	$2.40^{+0.45}_{-0.34}$		$0.386^{+0.061}_{-0.061}$	$0.046^{+0.016}_{-0.015}$	$1.97^{+0.71}_{-0.70}$	$0.935^{+0.048}_{-0.934}$	$2.8^{+2.7}_{-1.8}$	$10.5^{+5.5}_{-10.5}$
160–180	BB+PL	$2.15^{+0.29}_{-0.34}$		$0.193^{+0.032}_{-0.030}$	$0.020^{+0.011}_{-0.013}$	$5.2^{+2.3}_{-2.3}$	$0.953^{+0.042}_{-0.952}$	$3.3^{+7.0}_{-2.3}$	32^{+21}_{-32}

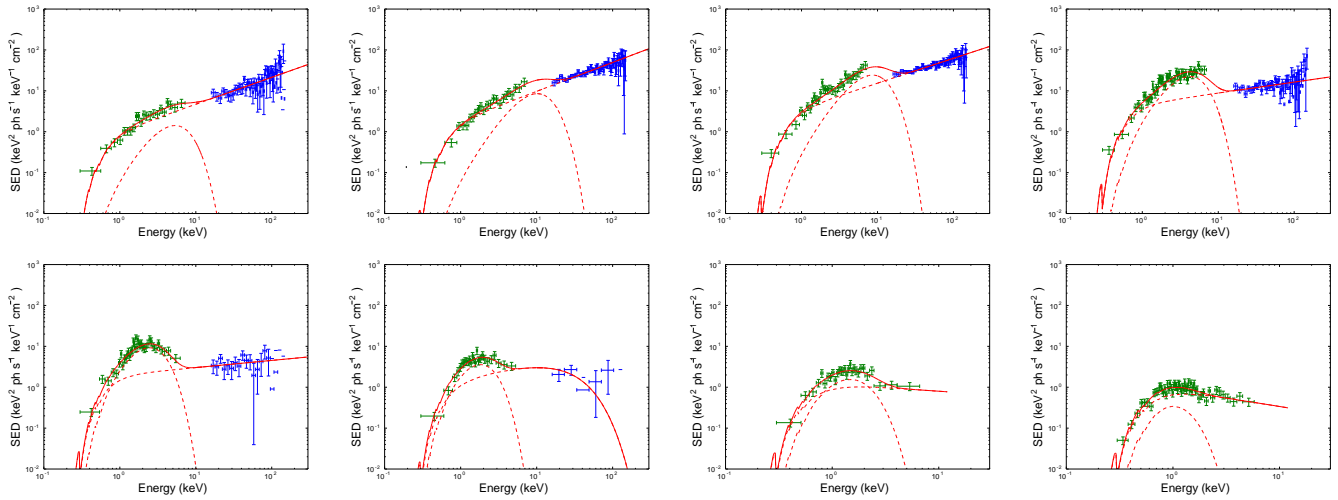


Figure 6. Gamma-ray flare: Time-resolved νF_ν spectra of the 8 time intervals in Tab. 1 (from the top left to the right and from the bottom left to the right). XRT data are displayed in green and BAT data in blue; BAT data points with no vertical lines corresponds to upper limits. Plots correspond to parameters obtained from minimum χ^2 fit.

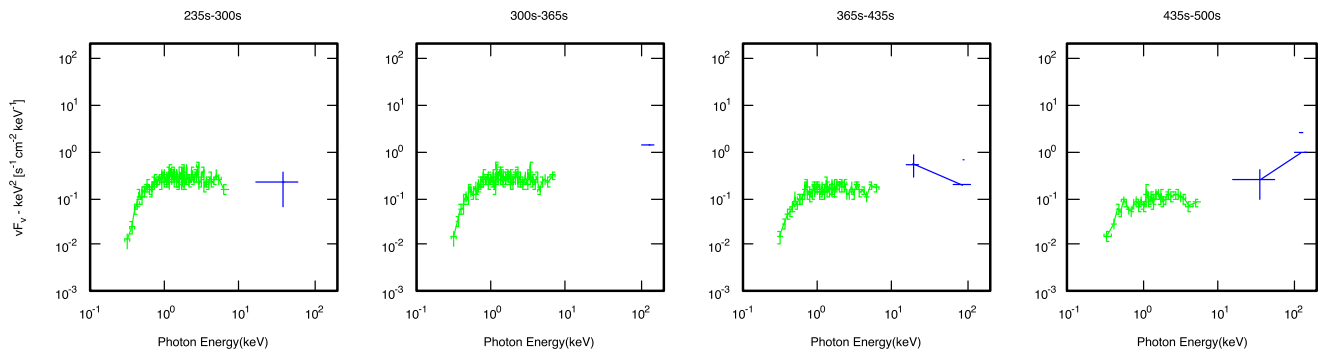


Figure 7. X-ray flare: Time-resolved BAT (blue) and XRT (green) νF_ν spectra of the X-ray flare in the indicated time intervals.

$E_c = 926 \pm 238$ keV. Such a cutoff can be caused by $\gamma\gamma$ absorption, for which the target photons energy is comparable to E_c , i.e., $E_c \gtrsim [\Gamma m_e c^2 / (1+z)]^2 / E_c$ and, therefore, the Lorentz factor can be deduced by

$$\Gamma \approx \frac{E_c}{m_e c^2} (1+z), \quad (1)$$

where m_e is the electron mass. From the above value of E_c , we infer $\Gamma = 3.28 \pm 0.84$, which represent an average over the Gamma-ray flare duration, which is in the range of the ones observed in thermal component (see the first five column of the Tab. 1), coinciding in turn with the numerical simulation of the interaction of the e^+e^- plasma with the SN ejecta described in the Sec. 5.

3.3. X-ray flare time-resolved analysis

We perform here also a time-resolved analysis of the X-ray flare. We divide the total interval Δt into four sub-intervals, i.e., 235–300 s, 300–365 s, 365–435 s and 435–500 s in the observer frame (see Fig. 7). The best-fits of each of these 4 time intervals are PL models with indexes ranging from -2.3 to -2.1 , which are consistent with the typical values inferred in (Ruffini et al. 2017b).

4. EVOLUTION OF THERMAL COMPONENT AROUND THE GAMMA-RAY FLARE

Following Ruffini et al. (2017b), in general, from the evolution of a thermal component it is possible to infer its expansion speed β (i.e., the velocity in units of the speed of light c). Assuming that the emitter is spherically symmetric and expands with a Lorentz gamma factor $\Gamma = (1 - \beta^2)^{-1/2}$, the effective emitter radius R in the laboratory frame is given by

$$R(\beta) = \Theta(\beta)^2 \Gamma \phi_0, \quad (2)$$

where the function $\Theta(\beta) \equiv 2[\beta(\beta - 1) + \ln(1 + \beta)]/\beta^2$ assumes the values $\Theta \rightarrow 1$ for $\beta \rightarrow 0$ and $\Theta \rightarrow 1.39$ for $\beta \rightarrow 1$. In Eq. 2 we define the quantity

$$\phi_0 = \frac{d_l}{(1+z)^2} \left(\frac{F_{\text{obs}}^{\text{bb}}}{\sigma T_{\text{obs}}^4} \right)^{1/2}, \quad (3)$$

in which $F_{\text{obs}}^{\text{bb}}$ and T_{obs} are the observed bolometric BB flux and temperature, respectively, and d_l the luminosity distance at the redshift z of the source. The evolutions of the rest-frame temperature and ϕ_0 are shown in Fig. 8. In astronomy the quantity ϕ_0 is usually identified with the radius of the emitter. However, in relativistic astrophysics this identity cannot be straightforwardly applied, because the estimate of the effective emitter radius R in Eq. 2 crucially depends on the knowledge

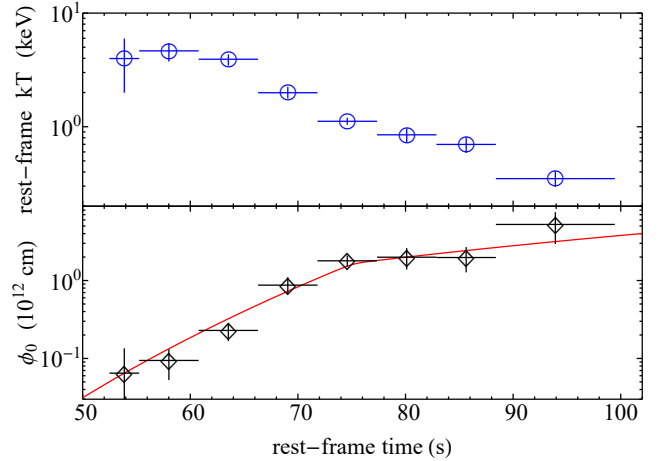


Figure 8. The cosmological rest-frame evolution of kT (upper panel) and ϕ_0 (bottom panel) of the thermal emitter in the Gamma-ray flare of GRB 151027A. The ϕ_0 interpolation (red line) is obtained by using two smoothly joined PL segments.

of its expansion velocity β (and, correspondingly, of Γ). This information can be deduced from the ratio between the variation of the emitter effective radius ΔR and the emission duration in laboratory frame Δt , i.e.

$$\beta = \frac{\Delta R}{c\Delta t} = \Theta(\beta)^2 \Gamma (1 - \beta \cos \vartheta) (1+z) \frac{\Delta \phi_0}{c\Delta t_a^d}, \quad (4)$$

where the laboratory time interval Δt relates to the corresponding arrival time intervals in the cosmological rest-frame Δt_a and in the observer frame Δt_a^d through (Bianco et al. 2001; Ruffini et al. 2001c):

$$\Delta t_a^d = \Delta t_a (1+z) = \Delta t (1 - \beta \cos \vartheta) (1+z), \quad (5)$$

where ϑ is the displacement angle of the considered photon emission point on the surface from the line of sight. In the following we consider only the case $\cos \vartheta = 1$.

To infer β , we fit the evolution of ϕ_0 (see Fig. 8 and Tab. 1) by using two smoothly joined PL segments. This allows us to estimate the ratio $\Delta \phi_0 / (c\Delta t_a^d)$ in Eq. 4 and, therefore, the values of β and Γ assuming that they are constant in each time interval (see Fig. 9, upper and middle panels). Consequently, we can estimate the evolution of the radius R of the emitter in the laboratory frame by taking into account the relativistic transformations described in Eqs. 2, 3 and 5 (see Fig. 9, lower panel). The results are summarized also in Tab. 1.

5. ON THE NATURE OF THE GAMMA-RAY AND THE X-RAY FLARES

Following the procedure described in Ruffini et al. (2017b), we interpret the thermal emission observed in the Gamma-ray flare as the observational feature arising from the early interaction between the expanding

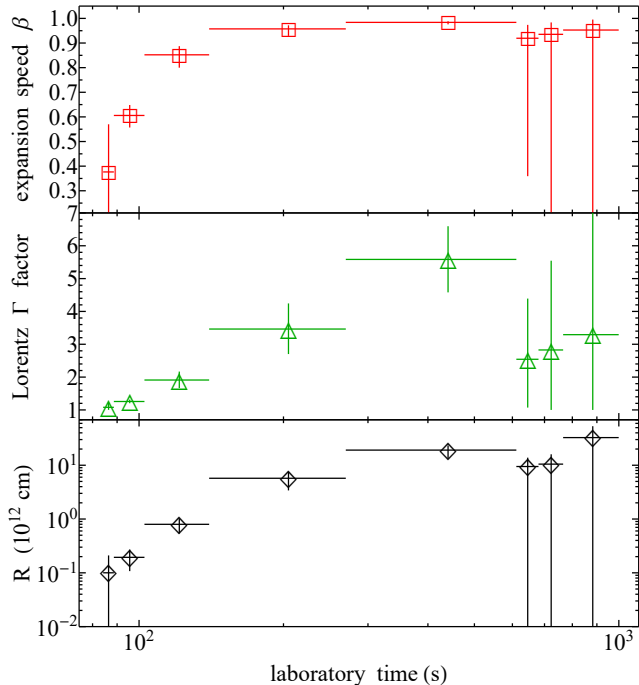


Figure 9. The evolution in the laboratory frame of β , Γ and R of the thermal emitter from the time intervals in Tab. 1.

SN ejecta and the e^+e^- plasma. a) We have performed simulations of such a process using the one-dimensional relativistic hydrodynamical (RHD) module included in the PLUTO¹ code (Mignone et al. 2011). In the spherically symmetric case considered, only the radial coordinate is used, and consequently the code integrates a system of partial differential equations in only two coordinates: the radius and the time. This permits the study of the evolution of the plasma along one selected radial direction at a time. The aforementioned equations are those of an ideal relativistic fluid, which can be written as follows:

$$\frac{\partial(\rho\Gamma)}{\partial t} + \nabla \cdot (\rho\Gamma\mathbf{v}) = 0, \quad (6)$$

$$\frac{\partial m_r}{\partial t} + \nabla \cdot (m_r\mathbf{v}) + \frac{\partial p}{\partial r} = 0, \quad (7)$$

$$\frac{\partial \mathcal{E}}{\partial t} + \nabla \cdot (\mathbf{m} - \rho\Gamma\mathbf{v}) = 0, \quad (8)$$

where ρ and p are the comoving fluid density and pressure, \mathbf{v} is the coordinate velocity in natural units ($c = 1$), $\Gamma = (1 - \mathbf{v}^2)^{-\frac{1}{2}}$ is the Lorentz gamma factor, $\mathbf{m} = h\Gamma^2\mathbf{v}$ is the fluid momentum, m_r its radial component, \mathcal{E} is the internal energy density measured in the comoving frame, and h is the comoving enthalpy density which is

defined by $h = \rho + \epsilon + p$. We define \mathcal{E} as follows:

$$\mathcal{E} = h\Gamma^2 - p - \rho\Gamma. \quad (9)$$

The first two terms on the right hand side of this equation coincide with the T^{00} component of the fluid energy-momentum, and the last one is the mass density in the laboratory frame.

Under the conditions discussed in Ruffini et al. (2017b), the plasma satisfies the equation of state of an ideal relativistic gas, which can be expressed in terms of its enthalpy as:

$$h = \rho + \frac{\gamma p}{\gamma - 1}, \quad (10)$$

with $\gamma = 4/3$. Imposing this equation of state closes and defines completely the system of equations, leaving as the only remaining freedom the choice of the matter density profile and the boundary conditions. To compute the evolution of these quantities in the chosen setup, the code uses the HLLC Riemann solver for relativistic fluids (see (Mignone et al. 2011)). Time evolution is performed by means of second-order Runge-Kutta integration, and a second-order total variation diminishing scheme is used for spatial interpolation. An adaptive mesh refinement algorithm is implemented as well, provided by the CHOMBO library (Colella et al. 2003). We turn now to the determination of the SN ejecta.

b) The e^+e^- plasma expands through the SN ejecta matter. The SN density and velocity profiles are taken from the 3D smoothed-particle-hydrodynamics (SPH)-like simulation of the SN ejecta expansion under the influence of the NS companion gravitational field. In our simulations we include the NS orbital motion and the NS gravitational-mass changes due to the accretion process modeled with the Bondi-Hoyle formalism (see Becerra et al. 2016, for more details). We set the SN ejecta initial conditions adopting an homologous velocity distribution in free expansion and the SN matter was modeled with 16 millions point-like particles. Each SN layer is initially populated following a power-law density profile of the CO_{core} as obtained from low-metallicity progenitors evolved with the Kepler stellar evolution code (Woosley et al. 2002). We take here as reference model the simulation of an initial binary system formed by a $2.0 M_\odot$ NS and a CO_{core} produced by a $M_{ZAMS} = 30 M_\odot$ progenitor. This leads to a total ejecta with mass $7.94 M_\odot$ and a ν NS of $1.5 M_\odot$. The orbital period of the binary is $P \approx 5$ min, i.e. a binary separation $a \approx 1.5 \times 10^{10}$ cm. The density profile exhibiting the evolution of the supernova ejecta and the companion star is shown in Fig. 10. Figure 11 shows the SN ejecta mass enclosed within a cone of 5 degrees of semi-aperture angle, and with

¹ <http://plutocode.ph.unito.it/>

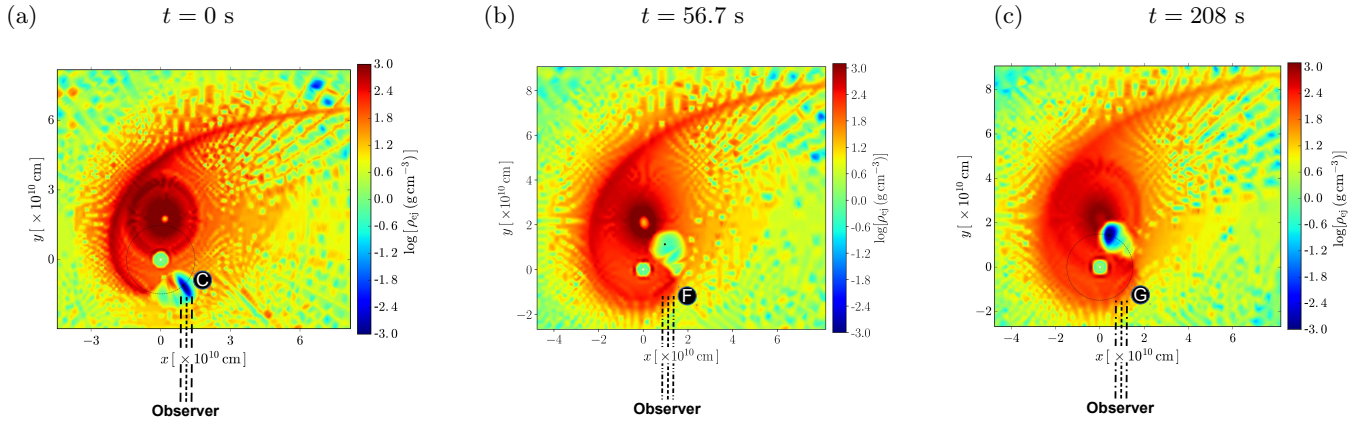


Figure 10. Three snapshots of the density distribution of the SN ejecta in the equatorial plane of the progenitor binary system. The time $t = 0$ indicates the instant when the NS companion reaches, by accretion, the critical mass and leads to the formation of a BH (black dot). The binary parameters of this simulations are: the NS companion has an initial mass of $2.0 M_{\odot}$; the CO_{core} , obtained from a progenitor with ZAMS mass $M_{\text{ZAMS}} = 30 M_{\odot}$, leads to a total ejecta mass $7.94 M_{\odot}$ and to a $1.5 M_{\odot}$ νNS (white dot), the orbital period is $P \approx 5$ min, i.e. a binary separation $a \approx 1.5 \times 10^{10}$ cm.

vertex at the position of the BH at the moment of its formation. The cone axis stands along the θ direction measured counterclockwise with respect to the line of sight. We simulate the interaction of the e^+e^- plasma with such ejecta from a radius $\approx 10^{10}$ cm all the way to $\approx 10^{12}$ cm where transparency is reached. We are currently running further SPH simulations of this process using the SNSPH code (Fryer et al. 2006) and will present the results in a forthcoming publication.

c) For the simulation of the Gamma-ray flare we set a total energy of the plasma equal to that of the Gamma-ray flare, i.e., $E_{\gamma} = 3.28 \times 10^{52}$ erg, and a baryon load $B = 79$, corresponding to a baryonic mass of $M_B = 1.45 M_{\odot}$. We obtain a radius of the transparency $R_{ph} = 4.26 \times 10^{11}$ cm, a Lorentz factor at transparency $\Gamma = 2.86$ and an arrival time of the corresponding radiation in the cosmological rest frame $t_a = 56.7$ s (see Fig. 12). This time is in agreement with the starting time of the Gamma-ray flare in the source rest-frame (see Sec. 2).

For the simulation of the the X-ray flare we set the energy $E_X = (4.4 \pm 2.9) \times 10^{51}$ erg as the total energy of the plasma and a baryon load $B = 590$, which corresponds to a baryonic mass of $M_B = 1.45 M_{\odot}$, we obtain a radius of the transparency $R_{ph} = 5.18 \times 10^{11}$ cm, a Lorentz gamma factor at transparency $\Gamma = 1.21$ and an arrival time of the corresponding radiation in the cosmological rest frame $t_a = 208$ s (see Fig. 13). This time is in agreement with the above time t_p at which the X-ray flare peaks in the rest frame.

6. DISCUSSION AND CONCLUSIONS

We have extended our recent treatment of analyzing the X-ray flare emission of 13 BdHNe (Ruffini et al. 2017b) to the prompt emission phase and the gamma-

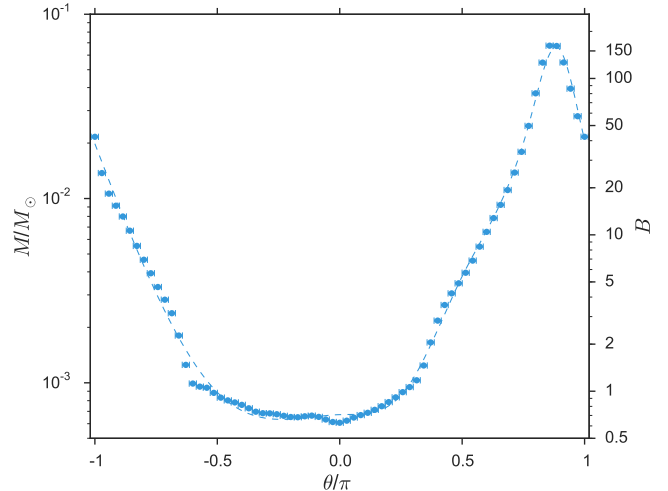


Figure 11. The SN ejecta mass enclosed within a cone of 5 degrees of semi-aperture angle and vertex positioned to an angle θ , measured counterclockwise, with respect to the line of sight (which passes through the νNS and BH at the moment of its formation; see Conclusions). The binary parameters of this simulations are: the NS has an initial mass of $2.0 M_{\odot}$; the CO_{core} obtained from a progenitor with ZAMS mass $M_{\text{ZAMS}} = 30 M_{\odot}$, leads to a total ejecta mass $7.94 M_{\odot}$, the orbital period is $P \approx 5$ min, i.e. a binary separation $a \approx 1.5 \times 10^{10}$ cm. The right-side vertical axis gives, as an example, the corresponding value of the baryon load B assuming a plasma energy of $E_{e^+e^-} = 1 \times 10^{53}$ erg.

ray flare in the specific case of GRB 151027A. This is a BdHN with excellent data from *Fermi* for the first 200 s, covering the prompt emission and the flares, and from *Swift* until 10^6 s, covering the prompt emission all the way to the latest phases of the afterglow.

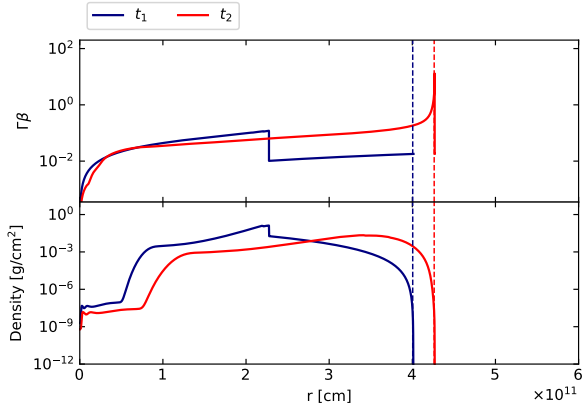


Figure 12. Numerical simulation of the Gamma-ray flare. We set a total energy of the plasma $E_\gamma = 3.28 \times 10^{52}$ erg and a baryon load $B = 79$, corresponding to a baryonic mass of $M_B = 1.45 M_\odot$. **Above:** Distribution of the velocity inside the SN ejecta at the two fixed values of the laboratory time t_1 (before the plasma reaches the external surface of the ejecta) and t_2 (the moment at which the plasma, after having crossed the entire SN ejecta, reaches the external surface). We plotted the quantity $\Gamma\beta$, recalling that we have $\Gamma\beta \sim \beta$ when $\beta < 1$ and $\Gamma\beta \sim \Gamma$ when $\beta \sim 1$. **Below:** Corresponding distribution of the mass density of the SN ejecta in the laboratory frame ρ_{lab} . We obtain a radius of the transparency $R_{ph} = 4.26 \times 10^{11}$ cm, a Lorentz factor at transparency $\Gamma = 2.86$ and an arrival time of the corresponding radiation in the cosmological rest frame $t_a = 56.7$ s.

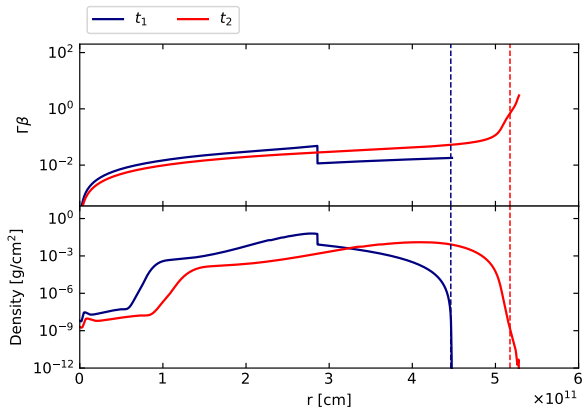


Figure 13. Numerical simulation of the X-ray flare. We set a total energy of the plasma $E_X = (4.4 \pm 2.9) \times 10^{51}$ erg and a baryon load $B = 590$, corresponding to a baryonic mass of $M_B = 1.45 M_\odot$. The plotted quantities are the same as in Fig. 12. We obtain a radius of the transparency $R_{ph} = 5.18 \times 10^{11}$ cm, a Lorentz factor at transparency $\Gamma = 1.21$ and an arrival time of the corresponding radiation in the cosmological rest frame $t_a = 208$ s.

Three main new results have been the outcome of our analysis:

- 1) We have found in the analysis of the prompt radiation, in the first 25 seconds a double component of gamma-ray spikes: one from -0.1 s to 9.6 s, the other from 17.5 s to 25 s; see Figs. 2 and 5. The first component fulfills all the properties of the prompt radiation: the presence of a PGRB, see Fig. 5(a), an ultra-relativistic Lorentz factor $\Gamma_0 = 503 \pm 76$, a baryon load $B = (1.92 \pm 0.35) \times 10^{-3}$, and a structure in the CBM with density $(15.9 \pm 3.2) \text{ cm}^{-3}$ extending to dimensions of 10^{16} cm, see Fig. 5(d). The second component appears to be surprisingly featureless. The understanding of the nature of these double spikes appear to be of the greatest interest since from a first look they appear to be also present in other systems such as GRB 140206A and GRB 160509A. We have reasons to consider seriously the possibility that this double component emission, unlike other processes related to the CBM, are connected to the nature of the formation of the BH.
- 2) The second result is the deep similarities and differences between the double component emission in the flares: the first component being the gamma-ray flare and the second the X-ray flare. Unexpectedly, no matter the large differences in energy, $E_\gamma = (3.28 \pm 0.13) \times 10^{52}$ erg for gamma-ray flares (Fig. 3) and $E_X = (4.4 \pm 2.9) \times 10^{51}$ erg for the X-ray flares (Fig. 4), both appear to have a same mildly relativistic regime already observed in Ruffini et al. (2017b), namely a Lorentz factor at transparency of $\Gamma \sim 5$ for the gamma-ray flare and a Lorentz factor of $\Gamma \sim 2$ for the X-ray flares. We then turn to the physical nature of these two processes, analyzed by our usual approach of the hydrodynamical equations describing that the interaction of e^+e^- plasma with the SN ejecta, see Fig. 12 for the gamma-ray flare and Fig. 13 for the X-ray flare. This leads to the result that the baryon load of the two flares are different, $B = 79$ for the gamma-ray flare and $B = 590$ for the X-ray flare. The two flares appear to be linked, as the difference in energy of the two sources is taken into account in the same value of the baryon mass of the ejecta, $M_B = 1.45 M_\odot$. This is visualized by the advanced simulations we have developed; see the three snapshots shown in Fig. 10.
- 3) The third result is equally rewarding in obtaining for the first time, using the correct general relativistic treatment described in Sec. 4 following

Ruffini et al. (2017b), the most clear identification of the transition from a SN moving at a speed of $0.38 c$ to and HN with a speed of $0.98 c$; see Fig. 9 and Tab. 1.

As already pointed out in our series of publications the common origin of all these process in the Prompt, in the gamma and X-ray flare originate in the e^+e^- plasma originating the GRBs. However, although their origin is common, their evolution is clearly acausal covering process and space-time evolution causally disconnected,

each leading to different world lines with a specific independent evolution, and leading to different Lorentz Gamma factors.

It is now challenging to show how such a mild-relativistic evolution in the plateau phases of BdHN, can indeed lead to a self-consistent theory of the afterglow. This is the subject of a different paper (Ruffini et al. 2017a). This alternative approach can be of importance for the explanation of the recent observations of the polarization in the plateau phase as well as of the double-peak structure in the prompt emission of GRB 160625B (Troja et al. 2017).

REFERENCES

- Becerra, L., Bianco, C. L., Fryer, C. L., Rueda, J. A., & Ruffini, R. 2016, *ApJ*, 833, 107
- Becerra, L., Cipolletta, F., Fryer, C. L., Rueda, J. A., & Ruffini, R. 2015, *ApJ*, 812, 100
- Bianco, C. L., Ruffini, R., & Xue, S.-S. 2001, *A&A*, 368, 377
- Colella, P., Graves, D. T., Johnson, J. N., et al. 2003, Chombo software package for AMR applications design document, Tech. Rep. LBNL-6615E
- Della Valle, M. 2011, *International Journal of Modern Physics D*, 20, 1745
- Dezalay, J.-P., Barat, C., Talon, R., et al. 1992, in *American Institute of Physics Conference Series*, Vol. 265, American Institute of Physics Conference Series, ed. W. S. Paciesas & G. J. Fishman, 304–309
- Fruchter, A. S., Levan, A. J., Strolger, L., et al. 2006, *Nature*, 441, 463
- Fryer, C. L., Rockefeller, G., & Warren, M. S. 2006, *ApJ*, 643, 292
- Fryer, C. L., Rueda, J. A., & Ruffini, R. 2014, *ApJ Letters*, 793, L36
- Goad, M. R., Osborne, J. P., Beardmore, A. P., & Evans, P. A. 2015, *GRB Coordinates Network*, 18482
- Golenetskii, S., Aptekar, R., Frederiks, D., et al. 2015, *GRB Coordinates Network*, 18516
- Izzo, L., Ruffini, R., Penacchioni, A. V., et al. 2012, *A&A*, 543, A10
- Klebesadel, R. W. 1992, *The durations of gamma-ray bursts*, ed. Ho, C., Epstein, R. I., & Fenimore, E. E., 161–168
- Kouveliotou, C., Meegan, C. A., Fishman, G. J., et al. 1993, *ApJ Letters*, 413, L101
- Maselli, A., D’Ai, A., Lien, A. Y., et al. 2015, *GRB Coordinates Network*, 18478
- Masumitsu, T., Negoro, H., Kawai, N., et al. 2015, *GRB Coordinates Network, Circular Service*, No. 18525, #1 (2015), 18525
- Mazets, E. P., Golenetskii, S. V., Ilinskii, V. N., et al. 1981, *Astrophysics and Space Science*, 80, 3
- Mignone, A., Zanni, C., Tzeferacos, P., et al. 2011, *The Astrophysical Journal Supplement Series*, 198, 7. <https://doi.org/10.1088%2F0067-0049%2F198%2F1%2F7>
- Nappo, F., Pescalli, A., Oganessian, G., et al. 2017, *A&A*, 598, A23
- Patricelli, B., Bernardini, M. G., Bianco, C. L., et al. 2012, *ApJ*, 756, 16
- Penacchioni, A. V., Ruffini, R., Izzo, L., et al. 2012, *A&A*, 538, A58
- Perley, D. A., Hillenbrand, L., & Prochaska, J. X. 2015, *GRB Coordinates Network*, 18487
- Romano, P., Campana, S., Chincarini, G., et al. 2006, *A&A*, 456, 917
- Rueda, J. A., & Ruffini, R. 2012, *ApJL*, 758, L7
- Ruffini, R. 1999, *A&A*, 138, 513
- Ruffini, R., Bernardini, M. G., Bianco, C. L., et al. 2006, in *American Institute of Physics Conference Series*, Vol. 836, *Gamma-Ray Bursts in the Swift Era*, ed. S. S. Holt, N. Gehrels, & J. A. Nousek, 103
- Ruffini, R., Bianco, C. L., Chardonnet, P., Frascchetti, F., & Xue, S. 2002, *ApJL*, 581, L19
- Ruffini, R., Bianco, C. L., Frascchetti, F., Xue, S.-S., & Chardonnet, P. 2001a, *ApJL*, 555, L117
- . 2001b, *ApJL*, 555, L113
- . 2001c, *ApJL*, 555, L107
- Ruffini, R., Karlica, M., Sahakyan, N., et al. 2017a, submitted to *ApJ*.
- Ruffini, R., Salmonson, J. D., Wilson, J. R., & Xue, S. 2000, *A&A*, 359, 855
- Ruffini, R., Vereshchagin, G., & Xue, S.-S. 2010, *PhR*, 487, 1
- Ruffini, R., Vitagliano, L., & Xue, S. 2003, *Physics Letters B*, 573, 33

- Ruffini, R., & Wilson, J. 1973, *Physical Review Letters*, 31, 1362
- Ruffini, R., Bernardini, M. G., Bianco, C. L., et al. 2007, in *ESA Special Publication*, Vol. 622, *ESA Special Publication*, 561
- Ruffini, R., Rueda, J. A., Muccino, M., et al. 2016, *ApJ*, 832, 136
- Ruffini, R., Wang, Y., Aimuratov, Y., et al. 2017b, *ArXiv e-prints*, arXiv:1704.03821
- Smith, N. 2014, *Annual Review of A&A*, 52, 487
- Smith, N., Li, W., Filippenko, A. V., & Chornock, R. 2011, *MNRAS*, 412, 1522
- Svensson, K. M., Levan, A. J., Tanvir, N. R., Fruchter, A. S., & Strolger, L.-G. 2010, *MNRAS*, 405, 57
- Tavani, M. 1998, *ApJL*, 497, L21
- Toelge, K., Yu, H.-F., & Meegan, C. A. 2015, *GRB Coordinates Network*, 18492
- Troja, E., Lipunov, V. M., Mundell, C. G., et al. 2017, *Nature*, 547, 425
- Woosley, S. E., & Bloom, J. S. 2006, *Annual Review of A&A*, 44, 507
- Woosley, S. E., Heger, A., & Weaver, T. A. 2002, *Reviews of Modern Physics*, 74, 1015
- Zel'dovich, Y. B., Ivanova, L. N., & Nadezhin, D. K. 1972, *Soviet Astronomy*, 16, 209